SCIENTIFIC REPORTS

OPEN

Determination of critical cooling rates in metallic glass forming alloy libraries through laser spike annealing

Punnathat Bordeenithikasem[1], Jingbei Liu[1], Sebastian A. Kube[1], Yanglin Li[1], Tianxing Ma[2], B. Ellen Scanley[3], Christine C. Broadbridge[3], Joost J. Vlassak[4], Jonathan P. Singer [2] & Jan Schroers[1]

The glass forming ability (GFA) of metallic glasses (MGs) is quantified by the critical cooling rate (R_C). Despite its key role in MG research, experimental challenges have limited measured R_C to a minute fraction of known glass formers. We present a combinatorial approach to directly measure R_C for large compositional ranges. This is realized through the use of compositionally-graded alloy libraries, which were photo-thermally heated by scanning laser spike annealing of an absorbing layer, then melted and cooled at various rates. Coupled with X-ray diffraction mapping, GFA is determined from direct R_C measurements. We exemplify this technique for the Au-Cu-Si system, where we identify $Au_{56}Cu_{27}Si_{17}$ as the alloy with the highest GFA. In general, this method enables measurements of R_C over large compositional areas, which is powerful for materials discovery and, when correlating with chemistry and other properties, for a deeper understanding of MG formation.

The glass forming ability (GFA) is most directly quantified by the inverse of the critical cooling rate (R_C), the minimum cooling rate required to avoid crystallization upon solidification resulting in vitrification into a fully amorphous state. Despite its significance, R_C has only been directly measured for a minute fraction of metallic glass (MG) forming systems[1–6]. The majority of R_C quantifications have been estimated using indirect methods. This is due to challenges in experimentally measuring R_C, particularly for glass formers with R_C exceeding $10^4\,K\,s^{-1}$. Therefore, a method to directly measure R_C would be both scientifically and technologically powerful. Even more impactful would be the ability to measure R_C over large composition ranges as it would enhance alloy development and provide insight into the mechanistic origins of glass formation.

Strategies to effectively consider large numbers of alloys are based on combinatorial synthesis paired with high-throughput characterization of properties. Such combinatorial strategies, well established in pharmaceutical research[7], are relatively new in materials science and particularly MG research. First combinatorial methods applied in MG research include measurements of mechanical properties[8–11], thermophysical properties[12–14], functional properties[15–17], thermoplastic formability[18], and microstructure evolution[11,12,19–21]. Attempts were made to draw conclusions about GFA from some of those measurements[10,12,18,21]. More recently approaches to measure GFA directly have been limited in cooling rate, in alloy composition, and generally in versatility[21–24].

In this study, we use a combinatorial approach to directly measure R_C across a significant fraction of the composition space in a ternary system. Through indirect laser spike annealing (LSA), we melt and cool co-sputtered alloy libraries over a range of controlled cooling rates. Employing structural and chemical characterization, R_C as a function of composition is determined and $Au_{56}Cu_{27}Si_{17}$ was identified as the alloy with the highest GFA in the Au-Cu-Si system.

[1]Department of Mechanical Engineering and Materials Science, Yale University, New Haven, Connecticut, 06511, USA. [2]Department of Mechanical and Aerospace Engineering, Rutgers University, Piscataway, New Jersey, 08854, USA. [3]Department of Physics, Southern Connecticut State University, New Haven, Connecticut, 06515, USA. [4]School of Engineering and Applied Science, Harvard University, Cambridge, Massachusetts, 02138, USA. Correspondence and requests for materials should be addressed to J.S. (email: jan.schroers@yale.edu)
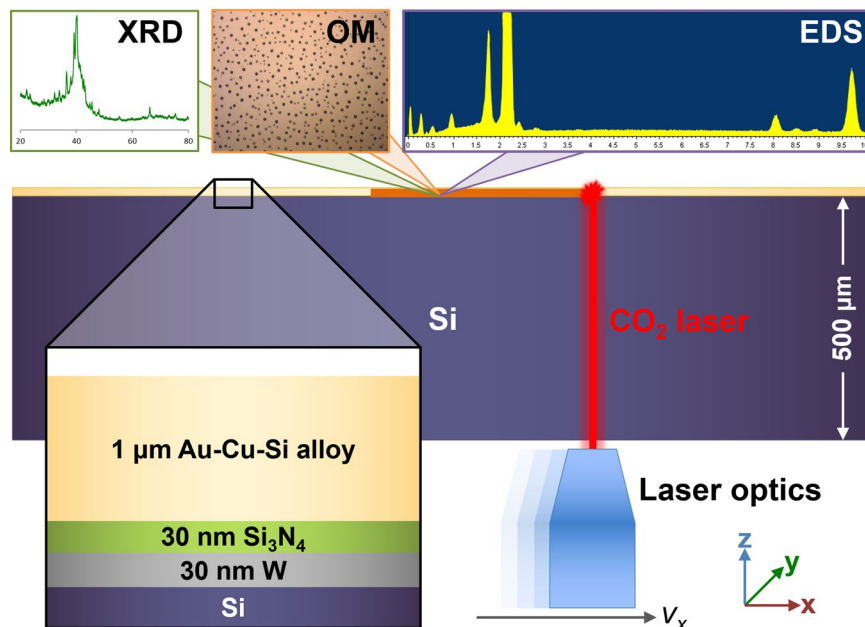
Figure 1. Schematic of the experimental setup for R_C measurements via laser spike annealing. We use a CO_2 laser with a 60 W continuous wave (CW) maximum output, operating at a wavelength of 10.6 μm. Compatible with this wavelength, intrinsic (undoped) Si, which has low absorption at 10.6 μm[32,51], is selected as the heat sink material. For the photo-thermal absorbing layer, we use 30 nm tungsten (W)[52], which is electrically insulated with 30 nm Si_3N_4 to prevent reflective thick film behavior[53] from the ~1 μm Au-Cu-Si ternary alloy library. This setup is mounted onto a fixture with adjustable height (z) for laser focus while the laser optics are motorized on two axes (x and y) such that the laser can be delivered to the substrate at known positions and scan speeds. Altering the laser scan speed, in this case v_x, varies the temperature profile. The samples are characterized using XRD, OM, and EDS mapping.

Results

Experimental setup for R_C measurements using laser heating.   To measure R_C, the synthesized alloy library must be melted and cooled in a controlled manner. Using LSA as a heating method provides localized, concentrated heat flux with precise control over the heating and cooling profile[25–28], which is ideal for combinatorial studies. However, directly exposing the laser onto an alloy film library can produce inconsistent temperature profiles. This is due to the composition-dependence of the absorption coefficient, which can vary significantly in a ternary system[29,30]. To avoid associated uncertainty in temperature and cooling rates, the alloy library is heated indirectly (Fig. 1). We realize this by co-sputtering the alloy library onto a substrate that is designed specifically for photo-thermal heating (see Methods). Such a substrate consists of a heat sink that is optically transparent to the laser and a photo-thermal absorbing layer. When the laser impinges on the substrate side, the radiation is transmitted through the heat sink and then absorbed by the absorbing layer, consequently heating the alloy via conduction. Tuning the incident laser heat flux via the laser scan speed determines the temperature profile, hence the cooling rate, experienced by the alloy.

Determination of cooling rates.   To demonstrate the proposed method, we first chose a film of constant composition $Au_{55}Cu_{25}Si_{20}$ (Fig. 2)[31]. Its composition was verified by energy dispersive X-ray spectroscopy (EDS). To vary the temperature profiles, the laser translational scan speed (v_x in Fig. 1) was systematically changed. X-ray diffraction (XRD) measurements, utilizing a beam mask commensurate to the heat affected zone size (2 mm), and optical microscopy (OM) were then carried out *ex-situ* (Fig. 2). For the slowest scan speed of 0.2 cm s^{-1}, large dendrites are observed (Fig. 2b) indicating melting and slow crystallization during cooling. XRD results reveal that with increasing laser scan speed, the amount of crystallinity and crystal size decreases.

To quantify the cooling rates for a given laser scan speed and power, simulations of the LSA process were conducted over the range of scan speeds where melting was visually observed and XRD measurements (Fig. 2a) on the remelted region indicated a transition from crystalline to amorphous. These simulations assumed a Gaussian-shaped heat source (see Methods). The laser power and peak width were determined by fitting the heat affected zone size, measured from OM images at different scan speeds (Fig. 2b–f), to produce the most representative simulations. The cooling rates could be extracted from the simulated temperature profiles of a particular point along the laser scan line (Fig. 2g). The cooling rate from the temperature profile that defines R_C is the cooling rate at the nose temperature (T_{Nose}) of the time-temperature-transformation (TTT) diagram. Across multiple Au-Cu-Si-based MG chemistries, T_{Nose} is approximately 0.8 times the liquidus temperature (T_L)[5,6,31]. Our simulations reveal a monotonic increase of the cooling rate with the laser scan speed (Fig. 2g inset), which is coupled with the maximum temperature (Fig. 2g). Hence, only scan speeds that result in maximum temperatures
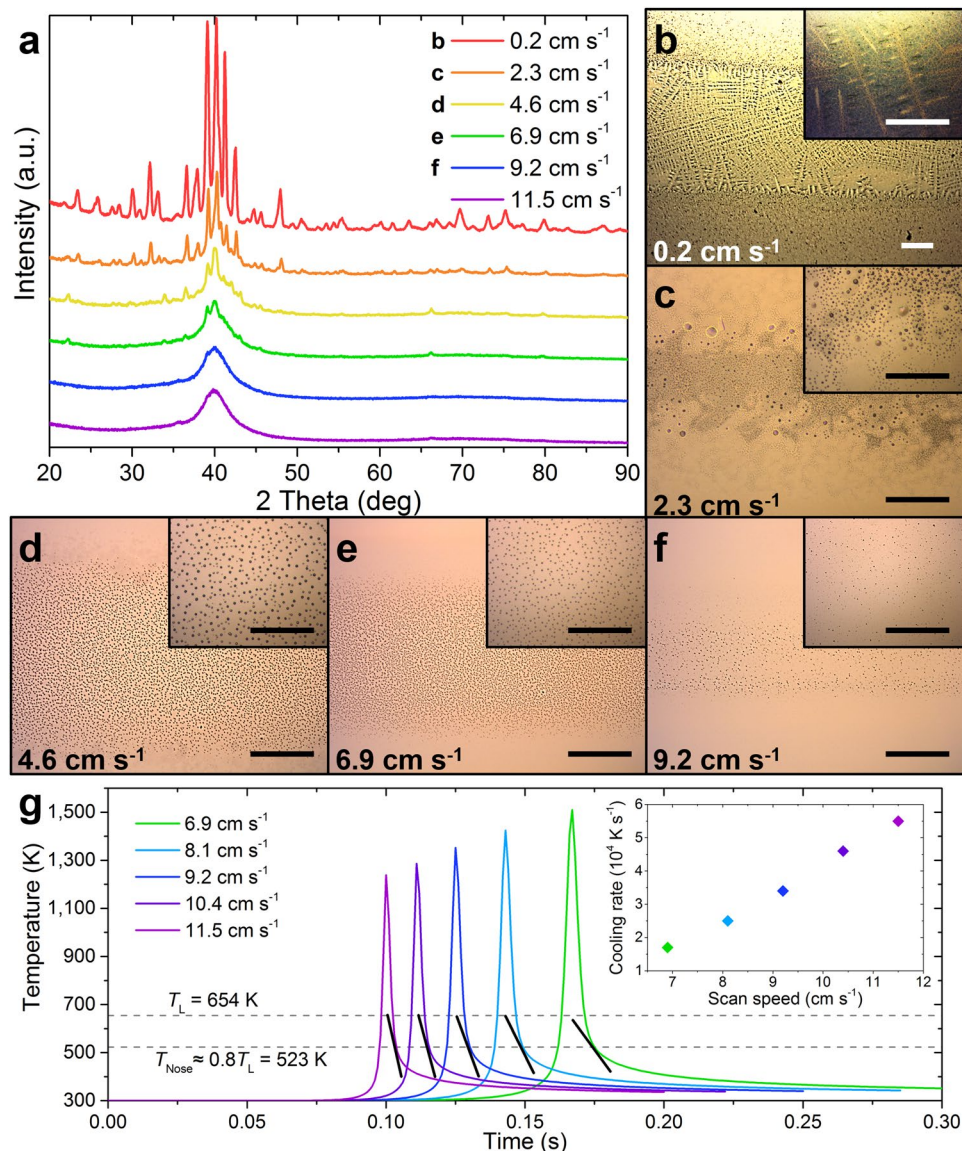
Figure 2. Determination of cooling rates at different laser scan speeds. (**a**) XRD diffractograms measured from $Au_{55}Cu_{25}Si_{20}$ films melted using multiple laser scan speeds. With higher scan speeds, the amorphous fraction increases, indicating faster cooling rates with faster scan speeds. (**b–f**) OM images, with a high magnification inset, of the $Au_{55}Cu_{25}Si_{20}$ film surface as a function of various laser scan speeds. Scale bars are 250 μm and 25 μm in the insets. For laser scan speeds exceeding 9.2 cm s^{-1}, the features are not clearly resolved by OM. The heat affected zone size is measured from the extent over which the microstructural features are observed in the direction perpendicular to the laser scan. (**g**) Simulated temperature profiles of laser heating experiments at variable scan speeds. The simulation was fitted with experimental values of the measured heat affected zone size. The T_L was taken from measured values of bulk samples of $Au_{55}Cu_{25}Si_{20}$[31] and T_{Nose} was approximated to be $0.8T_L$. The inset shows the calculated cooling rate at $0.8T_L$ as a function of laser scan speed.

exceeding T_L are considered. The R_C of $Au_{55}Cu_{25}Si_{20}$ MG is 3.4×10^4 K s^{-1}, as determined from the simulation for a scan speed of 9.2 cm s^{-1}.

It should be noted that the simulations do not consider the temperature-dependence of the absorption coefficient of Si, and therefore can be expected to slightly overestimate the cooling rate. These deviations are relatively low for relevant temperatures, as the optical absorption of Si[32] is four orders of magnitude lower than that of W[33] at T_L of $Au_{55}Cu_{25}Si_{20}$ (654 K)[31].

To ensure that the measured R_C reflects the intrinsic behavior of the alloy, one has to consider that at the outline of the heat affected zone resulting from LSA, a solid-liquid interface exists. Here, the unmelted solid could act as a nucleation site during solidification of the melted alloy. Whether or not this situation affects R_C measurements away from the interface can be concluded by the size of the solidifying grains, which has to be comparable to the melted zone size in order to significantly influence the observed R_C (Fig. 2b–f). This situation is only present at very slow cooling rates (Fig. 2b), much lower than the intrinsic R_C. Hence, we can conclude
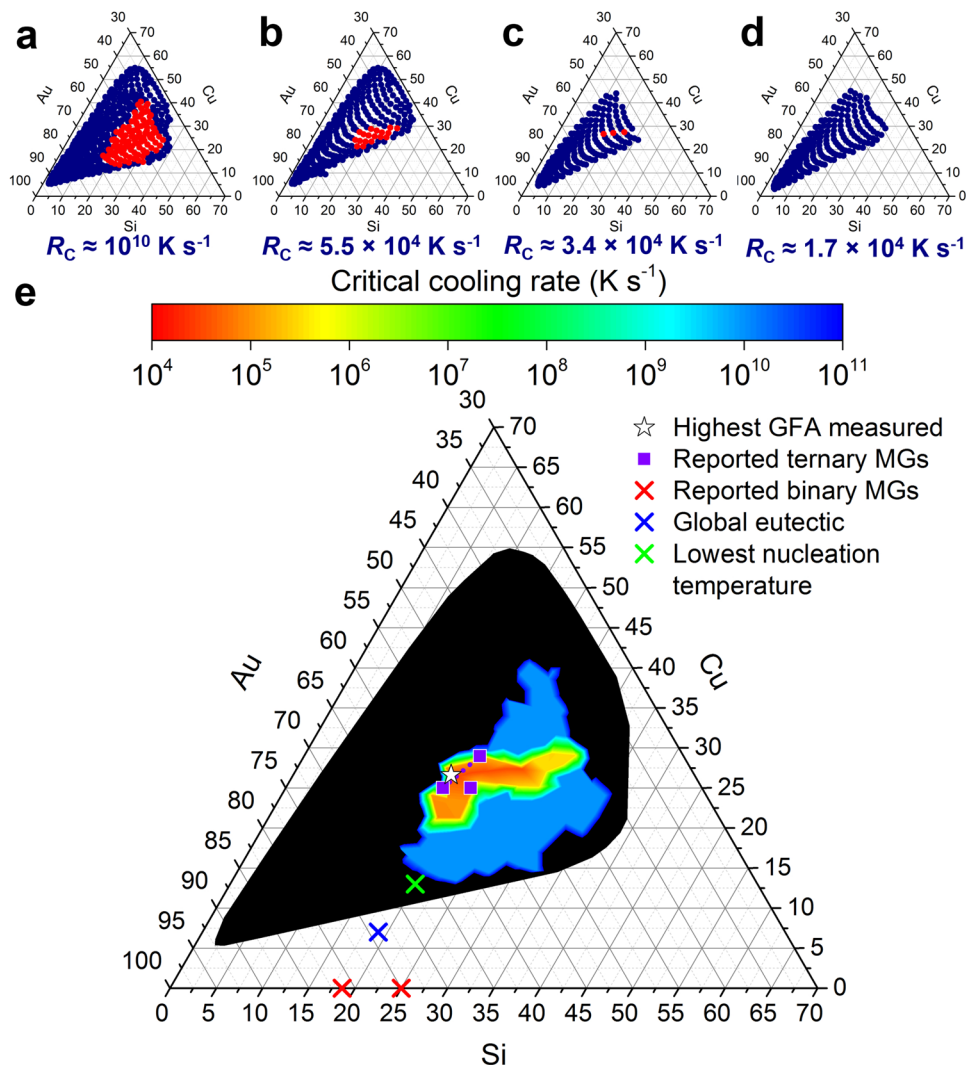
Figure 3. Composition-dependent R_C. Gibbs triangles with red circles depicting the fully amorphous state and navy blue circles depicting states with detectable crystalline phases of (**a**) as-sputtered films, which experienced a cooling rate of $10^{10}\,\mathrm{K\,s^{-1}}$, and films that have been laser-treated with scan speeds of (**b**) $11.5\,\mathrm{cm\,s^{-1}}$, (**c**) $9.2\,\mathrm{cm\,s^{-1}}$, and (**d**) $6.9\,\mathrm{cm\,s^{-1}}$. Based on temperature profile simulations (Fig. 2g), the R_C for the amorphous regions are approximately (**b**) $5.5 \times 10^4\,\mathrm{K\,s^{-1}}$, (**c**) $3.4 \times 10^4\,\mathrm{K\,s^{-1}}$, and (**d**) $1.7 \times 10^4\,\mathrm{K\,s^{-1}}$. (**e**) By compiling the mapped out regions of the amorphous phase as a consequence of multiple laser scan speeds (**a–d**), contours of R_C as a function of composition can be plotted. The black region represents considered compositions that crystallized, even upon sputtering. The symbols indicate the composition with the highest measured GFA, reported ternary MG compositions with high GFA[21,31] and dotted lines indicating a range, reported binary MG compositions[36,37], the global eutectic composition[34], and the composition with the lowest nucleation temperature[12]. The compositions in all the Gibbs triangles (**a–e**) are in at.%.

that the measured R_C is independent of the heterogeneous nucleation of from the solid-liquid interface, and is an innate property.

GFA as a function of composition.   The ultimate goal of the developed method is to determine R_C over large compositional regions. To realize such compositional regions, we fabricate compositional libraries by combinatorial co-sputtering from three sputtering guns in a tetrahedral arrangement[16,20]. Using this method we cover a composition range where Au varies from 32 to 93 at.%, Cu from 5 to 55 at.%, and Si from 1 to 39 at.%. Using EDS and XRD mapping, the composition and structure, respectively, as a function of position on the wafer is determined (Fig. 3). As-sputtered, the entire alloy library experienced a cooling rate of $\sim 10^{10}\,\mathrm{K\,s^{-1}}$. This is summarized in the Gibbs triangle indicating amorphous and crystalline regions (Fig. 3a). The as-sputtered state represents the fastest cooling rate in this investigation.

In order to determine R_C for the alloys with potentially the highest GFA in the Au-Cu-Si system, similar laser scan speeds that were used to determine R_C of $\mathrm{Au_{55}Cu_{25}Si_{20}}$ (Fig. 2) of 6.9, 9.2, and 11.5 $\mathrm{cm\,s^{-1}}$ were applied for LSA of the alloy libraries (Fig. 3b–d). The cooling rates near T_{Nose} that the amorphous regions were exposed to
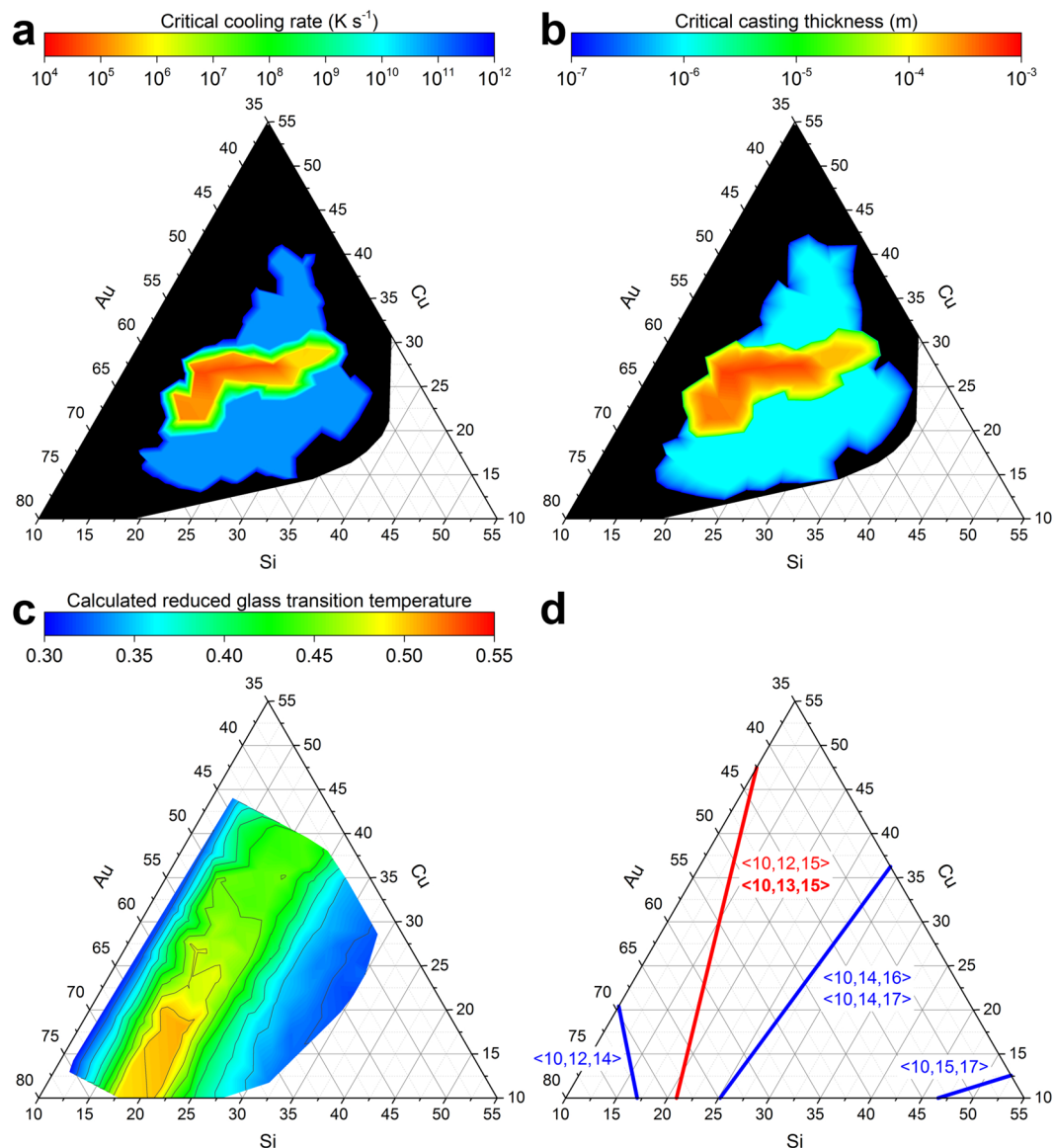
Figure 4. Comparison of composition-dependent GFA obtained from direct measurements with indirect GFA parameters (**a**) Contours of R_C as a function of composition. (**b**) The measured R_C is converted to d_C based on casting into a mold with infinite thermal mass and thermal conductivity, i.e. only the thermal properties of the melt were considered[39]. Given R_C in K s^{-1}, the d_C in meters is equal to $\sqrt{\frac{0.01}{R_C}}$. (**c**) $T_{rg} = T_g/T_L$ where T_g was estimated[41] by first calculating the elastic moduli[42,43] and calibrating with a known T_g that was determined by calorimetry[31] (calculation details discussed in caption of Supplementary Fig. 1), while T_L was extracted from the ternary liquidus projection[34]. (**d**) Applying an efficient cluster-packing structural model for metallic glasses[45], 100% efficiently packed lines for various $<Z_{Si,tot}, Z_{Cu,tot}, Z_{Au,tot}>$ structures were calculated for the composition region of interest. Indicated as a red line is the $<10, 13, 15>$ structure, which is recommended by the authors of the model[45] for the Au-Cu-Si system.

are 1.7×10^4 K s^{-1}, 3.4×10^4 K s^{-1}, and 5.5×10^4 K s^{-1}, respectively. For a scan speed of 11.5 cm s^{-1}, the amorphous region shrank significantly in comparison to the one for the as-sputtered data. For example, the maximum of Au variation over which the library remains amorphous reduces from 39 to 66 at.% to 42 to 60 at.%. When the scan speed is further decreased to 9.2 cm s^{-1}, the amorphous region narrows further such that only the best glass formers in the compositional space vitrify upon solidification. Here the range in Au content is only 48 to 56 at.%. Vitrified alloys from the 9.2 cm s^{-1} scan speed have R_C values comparable to Au$_{55}$Cu$_{25}$Si$_{20}$. For a scan speed of 6.9 cm s^{-1}, all considered alloys crystallize.

Across multiple laser scan speeds, R_C can be calculated from the slowest laser scan speed applied to vitrify the alloy. Once the slowest laser scan speed is determined, the numerical value of R_C is obtained as the cooling rate at $0.8T_L$ from the corresponding simulation (Fig. 2g). T_L is extracted from the ternary phase diagram[34]. As the final result, R_C is plotted as a function of composition (Figs 3e and 4a).

Discussion

The GFA for a large compositional space was directly determined using XRD and EDS mapping of alloy libraries heated with lasers at multiple scan speeds (Figs 3e and 4a). Upon sputtering, the composition range of Au between 39 to 66 at.%, Cu between 13 to 41 at.%, and Si 16 to 35 at.% forms the amorphous phase. The region of the highest GFA ($R_C \leq 3.4 \times 10^4 \, K \, s^{-1}$) spans from $Au_{56}Cu_{27}Si_{17}$, along the approximately constant Cu line until $Au_{48}Cu_{28}Si_{24}$. This region coincides, within margins of error, with $Au_{55}Cu_{25}Si_{20}$, which is the alloy with the highest previously reported GFA as determined through cumbersome and numerous trial-and-error experiments[31]. The results are also consistent with the region of highest GFA determined by nanocalorimetry, which is the range between $Au_{58}Cu_{25}Si_{17}$ and $Au_{52}Cu_{29}Si_{19}$[21].

From our results, we can draw conclusions about the change of GFA with composition. When the Cu content is maintained between 25 to 30 at.%, R_C is less sensitive to the Si concentration; R_C increases gradually from $3.4 \times 10^4 \, K \, s^{-1}$ to about $3 \times 10^5 \, K \, s^{-1}$ when Si content increases from 17 to 29 at.% and then R_C increases rapidly to over $10^{10} \, K \, s^{-1}$ when the Si concentration is 31 at.% or higher. On the low Si side, GFA drops abruptly once the Si content drops below 16 at.%. For the most extreme case, R_C changes from $3.4 \times 10^4 \, K \, s^{-1}$ to over $10^{10} \, K \, s^{-1}$ when the Si concentration decreases from 17 to 15 at.%. This implies that within a 2 at.% composition difference, R_C can change by as much as six orders of magnitude. The degree of variations in GFA with composition are much larger than the variations recently reported for metal-metalloid glass formers[35]. However, it is conceivable that for the proposed method, particularly for this example system, some alloys crystallized rapidly even at ambient or sputtering temperatures (~293 to 323 K). Hence, an alloy that vitrified upon sputtering may have crystallized prior to characterization and would be identified as crystalline upon sputtering. Obviously, this situation is more likely to occur in alloys with glass transition temperatures (T_g) in the vicinity of ambient temperatures such as for binary Au-Si glasses[36]. Evidence for such a scenario is the fact that $Au_{75}Si_{25}$[37] and $Au_{81.4}Si_{18.6}$[36] have both been reported to vitrify upon splat quenching (~$10^6 \, K \, s^{-1}$ [38]), whereas sputtered (~$10^{10} \, K \, s^{-1}$) Au-Si alloys are identified as crystalline. Hence, the composition-dependence of GFA, measured using the proposed method, should be carried out for alloy regions where T_g is significantly larger than ambient temperature, arguably >340 K (Supplementary Fig. 1).

R_C can be converted to the critical casting thickness (d_C), the maximum thickness that a material can be made fully amorphous via quenching[39]; an often more practical measure (Fig. 4b). For Au-Cu-Si alloys with the highest GFA (R_C of $3.4 \times 10^4 \, K \, s^{-1}$), the d_C is calculated to be 540 μm, consistent with reported values[31]. This confirms the proposed approach and indicates that there is no ternary bulk ($d_C \geq 1$ mm) MG (BMG) in the Au-Cu-Si system.

The availability of R_C over such a large and unprecedented range of compositions (Figs 3e and 4a) makes it possible to test the validity of indicators of GFA that are widely used and provide insight into motives for glass formation. The reduced glass transition temperature ($T_{rg} = T_g/T_L$), proposed by Turnbull, has been suggested to correlate directly with GFA[40]. However, like for most GFA indicators, T_{rg} relies on parameters that are not known *a priori* and therefore have to be estimated (Fig. 4c). Here, T_g was estimated[41] as a function of composition by initially calculating the elastic moduli[42,43] then correlating the elastic moduli values to T_g which in turn was calibrated with a known T_g determined by calorimetry[31]; T_L was obtained from the liquidus projection of the ternary phase diagram[34]. In the composition range under consideration, the estimated T_g values span from 326 to 376 K (Supplementary Fig. 1), consistent with experimentally determined values[44]. Because the variation in T_g is significantly less than the variation in T_L, the composition dependence of T_{rg} is primarily dictated by the change in T_L.

Based on T_{rg}, alloys with high GFA are expected to be near eutectic compositions. This is consistent with our reported findings (Figs 3e and 4a). The range of high GFA ($R_C \leq 10^5 \, K \, s^{-1}$) corresponds to regions where T_{rg} is above 0.4, i.e. between 14 and 27 at.% Si. Moving towards low Si concentrations, at ~15 at.%, the rapid drop in the measured GFA coincides with a steep decline in T_{rg}. At the higher Si concentrations, the GFA drop is more gradual, despite a substantial decrease in T_{rg}. Overall, the trends predicted by T_{rg} agree broadly with the experimental GFA, although deviations as large as 10 at.% are possible. For example, the composition region of maximum T_{rg} does not coincide with the compositions of maximum GFA determined experimentally.

A recently proposed model[45], based on efficient cluster-packing, has also been tested against the experimentally determined composition dependence of R_C (Fig. 4d). In short, the model identifies compositions and atomic size differences such that packing clusters are simultaneously efficiently packed about each constituent element. For ternary systems, the most efficiently packed structures form a line in the Gibbs triangle[45].

The lines of 100% efficiently packed structures were calculated for compositions in the vicinity of the glass-forming range (Fig. 4d)[45,46]. The notation for indicating cluster packing structures is $<Z_{Si,tot}, Z_{Cu,tot}, Z_{Au,tot}>$, where $Z_{i,tot}$ is the total number of atoms present in the first shell of a cluster centered about element i. The $<10, 13, 15>$ structure has been suggested to represent Au-Cu-Si glass formers[45]. This line coincides with the line for the $<10, 12, 15>$ structure and does indeed intersect with the center of the experimentally determined glass-forming range. Other structures, namely $<10, 14, 16>$ and $<10, 14, 17>$ coincide with the periphery of the experimentally determined glass-forming range. However, the line for the structure predicted by the efficient cluster-packing model, $<10, 12, 14>$, did not intersect with any glass formers. This comparison suggests that efficient cluster-packing model can assist in reducing the overall composition space, however this reduction is small.

In order to evaluate the effectiveness, practicality, and speed of the proposed technique to experimentally measure GFA over large composition ranges, a comparison with the total number of potential bulk glass forming alloys has to be made. It has been estimated that the number of potential BMG forming alloys is on the order of 10^6 alloys out of 10^{12} unique alloys with two to five constituent elements[47]. Assuming a fabrication rate of 1000 alloys per day with the proposed method, it would still require over 2,700,000 years to synthesize and characterize the entire alloy space. This comparison suggests that prior to the combinatorial method, a significant reduction in the composition space is required to tackle the complex phenomena of glass formation and to identify many of the yet to be discovered MG and BMG alloys. Here, using theoretical predictions based on parameters that are known *a priori* to identify glass forming systems and reduce the composition space of interest will be powerful[48].

Subsequently these suggested composition ranges would be characterized with our proposed combinatorial method to identify MG and BMG formers. In a final step, a small number of selected alloys, which are suggested by the combinatorial method, would be fabricated in bulk form and characterized by using highly precise and established bulk characterization methods. Thus, the proposed method can be considered the missing link for effective MG discovery.

Methods

Sample Fabrication, Laser Heating, and Characterization. The layered film structure is fabricated by confocal DC magnetron co-sputtering (AJA International ATC 2200) with elemental targets with purity exceeding 99.95%. The sputtering guns are arranged in a tetrahedral arrangement at a default angle of 29.8 degrees from the vertical. Prior to any sputtering step, a base pressure level of 10^{-6} Pa and a working pressure of 0.3 Pa of flowing ultra high purity (UHP) Ar is achieved. The substrates were 100 mm diameter, 500 μm thick, double-side polished, intrinsic Si wafers (UniversityWafer, Inc.). Firstly, 30 nm of W was sputtered at 70 W power. Then, 30 nm of Si_3N_4 was sputtered by reactive sputtering, using a Si sputtering gun at 70 W under flowing UHP Ar and additionally flowing 10 standard $cm^3 min^{-1}$ of UHP N_2 gas. Finally, 1 μm of Au-Cu-Si alloy is co-sputtered with powers of 41 W, 37 W, and 175 W for Au, Cu, and Si, respectively. For a constant composition film, the substrate is rotated during the sputtering process. To fabricate alloy libraries with compositional gradients, the substrates are left stationary. Changing the sputtering power and tilt angles of each specific sputtering gun would alter the compositional spread of the libraries.

The as-sputtered alloy film is first characterized with automated XRD (Rigaku Smartlab) using Cu Kα radiation with a 2 mm beam mask and automated EDS (Oxford Instruments X-Max detector attached to a Zeiss Sigma VP Field Emission scanning electron microscope) to determine the structure and composition, respectively, as a function of position on the wafer. Next, the sample undergoes LSA using a 60 W CO_2 laser (Universal Laser Systems VLS 6.60) at a set laser scan speed, incident from the heat sink (Si wafer) side. The laser scan lines are spaced 5 mm apart center-to-center to avoid heat affected zone interactions. Finally, the sample is then characterized with XRD and OM (Nikon ME600 with ThorLabs CCD camera).

Temperature profile simulations. Temperature profile simulations were done using the commercial package COMSOL Multiphysics® for time-dependent thermal finite element method simulations, informed by the experimental results. A 100 mm intrinsic Si wafer was modeled using temperature-dependent thermal conductivity, density, and specific heat capacity[49]. The wafer is assumed to be thermally isotropic. All surfaces are air-cooled with no forced convection ($h = 5$). Ambient temperature and the wafer edge were assumed to be 300 K. The laser was modeled as a Gaussian-shaped surface heat source, where the peak width and power was fitted with experimental measurements of the heat-affected zone size, which was measured using the OM images with ImageJ[50] software. The thin photo-thermal and alloy layers, having high thermal diffusivities and low thermal masses, are assumed to be isothermal to the top surface of the Si wafer. The temperature profiles for different scan speeds (Fig. 2g) were recorded from one fixed point, located 1.27 cm from the origin of laser incidence and along the path of the laser scan to allow time to reach a stable temperature.

Data Availability. The datasets generated during and/or analyzed during the current study are available from the corresponding author on reasonable request.

References

1. Nishiyama, N. & Inoue, A. Supercooling investigation and critical cooling rate for glass formation in Pd–Cu–Ni–P alloy. *Acta Materialia* **47**, 1487–1495 (1999).
2. Mukherjee, S., Schroers, J., Johnson, W. L. & Rhim, W. K. Influence of Kinetic and Thermodynamic Factors on the Glass-Forming Ability of Zirconium-Based Bulk Amorphous Alloys. *Physical Review Letters* **94**, 245501 (2005).
3. Zhong, L., Wang, J., Sheng, H., Zhang, Z. & Mao, S. X. Formation of monatomic metallic glasses through ultrafast liquid quenching. *Nature* **512**, 177–180 (2014).
4. Pogatscher, S., Leutenegger, D., Hagmann, A., Uggowitzer, P. J. & Löffler, J. F. Characterization of bulk metallic glasses via fast differential scanning calorimetry. *Thermochimica Acta* **590**, 84–90 (2014).
5. Pogatscher, S., Uggowitzer, P. J. & Löffler, J. F. *In-situ* probing of metallic glass formation and crystallization upon heating and cooling via fast differential scanning calorimetry. *Applied Physics Letters* **104**, 251908 (2014).
6. Bai, F. X., Yao, J. H., Wang, Y. X., Pan, J. & Li, Y. Crystallization kinetics of an Au-based metallic glass upon ultrafast heating and cooling. *Scripta Materialia* **132**, 58–62 (2017).
7. Macarron, R. *et al.* Impact of high-throughput screening in biomedical research. *Nature Reviews Drug Discovery* **10**, 188–195 (2011).
8. Schnabel, V. *et al.* Revealing the relationships between chemistry, topology and stiffness of ultrastrong Co-based metallic glass thin films: A combinatorial approach. *Acta Materialia* **107**, 213–219 (2016).
9. Guo, Q. *et al.* Compositional dependence of Young's moduli for amorphous Cu–Zr films measured using combinatorial deposition on microscale cantilever arrays. *Scripta Materialia* **64**, 41–44 (2011).
10. Li, Y., Guo, Q., Kalb, J. A. & Thompson, C. V. Matching Glass-Forming Ability with the Density of the Amorphous Phase. *Science* **322**, 1816–1819 (2008).
11. Deng, Y. P. *et al.* A combinatorial thin film sputtering approach for synthesizing and characterizing ternary ZrCuAl metallic glasses. *Intermetallics* **15**, 1208–1216 (2007).
12. Ding, S., Gregoire, J., Vlassak, J. J. & Schroers, J. Solidification of Au-Cu-Si alloys investigated by a combinatorial approach. *Journal of Applied Physics* **111**, 114901–114906 (2012).
13. McCluskey, P. J. & Vlassak, J. J. Glass transition and crystallization of amorphous Ni–Ti–Zr thin films by combinatorial nano-calorimetry. *Scripta Materialia* **64**, 264–267 (2011).
14. McCluskey, P. J. & Vlassak, J. J. Combinatorial nanocalorimetry. *Journal of Materials Research* **25**, 2086–2100 (2010).
15. Ryusuke, Y., Seiichi, H., Junpei, S. & Akira, S. Combinatorial Search for Low Resistivity Pd–Cu–Si Thin Film Metallic Glass Compositions. *Japanese Journal of Applied Physics* **45**, 5911 (2006).
16. Liu, Y. *et al.* Combinatorial development of antibacterial Zr-Cu-Al-Ag thin film metallic glasses. *Scientific Reports* **6**, 26950 (2016).
17. Doubek, G. *et al.* Guided Evolution of Bulk Metallic Glass Nanostructures: A Platform for Designing 3D Electrocatalytic Surfaces. *Advanced Materials* (2015).

18. Ding, S. *et al*. Combinatorial development of bulk metallic glasses. *Nature Materials* **13**, 494–500 (2014).
19. Sakurai, J., Hata, S., Yamauchi, R. & Shimokohbe, A. Combinatorial arc plasma deposition search for Ru-based thin film metallic glass. *Applied Surface Science* **254**, 720–724 (2007).
20. Li, Y. *et al*. Combinatorial Strategies for Synthesis and Characterization of Alloy Microstructures over Large Compositional Ranges. *ACS Combinatorial Science* **18**, 630–637 (2016).
21. Gregoire, J. M. *et al*. Combining combinatorial nanocalorimetry and X-ray diffraction techniques to study the effects of composition and quench rate on Au–Cu–Si metallic glasses. *Scripta Materialia* **66**, 178–181 (2012).
22. Tsai, P. & Flores, K. M. A combinatorial strategy for metallic glass design via laser deposition. *Intermetallics* **55**, 162–166 (2014).
23. Tsai, P. & Flores, K. M. A Laser Deposition Strategy for the Efficient Identification of Glass-Forming Alloys. *Metallurgical and Materials Transactions A* **46**, 3876–3882 (2015).
24. Tsai, P. & Flores, K. M. High-throughput discovery and characterization of multicomponent bulk metallic glass alloys. *Acta Materialia* **120**, 426–434 (2016).
25. Harris, T. R. Optical properties of Si, Ge, GaAs, GaSb, InAs, and InP at elevated temperatures. Air Force Institute of Technology (2010).
26. Green, M. A. & Keevers, M. J. Optical properties of intrinsic silicon at 300 K. *Progress in Photovoltaics: Research and Applications* **3**, 189–192 (1995).
27. Zhou, X., Zhao, A., Yuan, M. & Yu, X. Study on infrared absorption of tungsten nanofilms. *SPIE Proceedings* **8202**, 820217 (2011).
28. Lang, W., Kühl, K. & Sandmaier, H. Absorbing layers for thermal infrared detectors. *Sensors and Actuators A: Physical* **34**, 243–248 (1992).
29. Wang, X., Bellouard, Y. & Vlassak, J. J. Laser annealing of amorphous NiTi shape memory alloy thin films to locally induce shape memory properties. *Acta Materialia* **53**, 4955–4961 (2005).
30. Jung, B. *et al*. Sub-millisecond post exposure bake of chemically amplified resists by CO_2 laser heat treatment. *SPIE Proceedings* **7639**, 76390L (2010).
31. Singer, J. P. *et al*. Alignment and reordering of a block copolymer by solvent-enhanced thermal laser direct write. *Polymer* **55**, 1875–1882 (2014).
32. Singer, J. P., Kooi, S. E. & Thomas, E. L. Focused laser spike (FLaSk) annealing of photoactivated chemically amplified resists for rapid hierarchical patterning. *Nanoscale* **3**, 2730–2738 (2011).
33. Cretu, C. & van der Lingen, E. Coloured gold alloys. *Gold Bulletin* **32**, 115–126 (1999).
34. Liu, J. *et al*. Combinatorial exploration of color in gold-based alloys. *Gold Bulletin* **48**, 111–118 (2015).
35. Schroers, J., Lohwongwatana, B., Johnson, W. L. & Peker, A. Gold based bulk metallic glass. *Applied Physics Letters* **87**, 061912 (2005).
36. Ordal, M. A., Bell, R. J., Alexander, R. W., Newquist, L. A. & Querry, M. R. Optical properties of Al, Fe, Ti, Ta, W, and Mo at submillimeter wavelengths. *Applied Optics* **27**, 1203–1209 (1988).
37. Chen, H. S. & Turnbull, D. Thermal Properties of Gold-Silicon Binary Alloy near the Eutectic Composition. *Journal of Applied Physics* **38**, 3646–3650 (1967).
38. Klement, W., Willens, R. H. & Duwez, P. O. L. Non-crystalline Structure in Solidified Gold-Silicon Alloys. *Nature* **187**, 869–870 (1960).
39. Villars, P. & Okamoto, H. Au-Cu-Si Liquidus Projection of Ternary Phase Diagram: Datasheet from "PAULING FILE Multinaries Edition – 2012" in SpringerMaterials (http://materials.springer.com/isp/phase-diagram/docs/c_1500096). Springer-Verlag Berlin Heidelberg & Material Phases Data System (MPDS), Switzerland & National Institute for Materials Science (NIMS), Japan.
40. Lin, X. H. & Johnson, W. L. Formation of Ti–Zr–Cu–Ni bulk metallic glasses. *Journal of Applied Physics* **78**, 6514–6519 (1995).
41. Wang, W. H. Elastic moduli and behaviors of metallic glasses. *Journal of Non-Crystalline Solids* **351**, 1481–1485 (2005).
42. Wang, W. H. Correlations between elastic moduli and properties in bulk metallic glasses. *Journal of Applied Physics* **99**, 093506 (2006).
43. Callister, W. D., Rethwisch, D. G. *Materials Science and Engineering: An Introduction*, Ninth edn. Wiley (2014).
44. Laws, K. J., Miracle, D. B. & Ferry, M. A predictive structural model for bulk metallic glasses. *Nature Communications* **6**, 8123 (2015).
45. Na, J. H. *et al*. Compositional landscape for glass formation in metal alloys. *Proceedings of the National Academy of Sciences* **111**, 9031–9036 (2014).
46. Ruhl, R. C. Cooling rates in splat cooling. *Materials Science and Engineering* **1**, 313–320 (1967).
47. Turnbull, D. Under what conditions can a glass be formed? *Contemporary Physics* **10**, 473–488 (1969).
48. Wang, C., Liao, Y.-C., Chu, J. P. & Hsueh, C.-H. Viscous flow and viscosity measurement of low-temperature imprintable AuCuSi thin film metallic glasses investigated by nanoindentation creep. *Materials & Design* **123**, 112–119 (2017).
49. Miracle, D. B., Sanders, W. S. & Senkov, O. N. The influence of efficient atomic packing on the constitution of metallic glasses. *Philosophical Magazine* **83**, 2409–2428 (2003).
50. Li, Y., Zhao, S., Liu, Y., Gong, P. & Schroers, J. How many bulk metallic glasses are there? *Personal Communication* (2017).
51. Miracle, D., Majumdar, B., Wertz, K. & Gorsse, S. New strategies and tests to accelerate discovery and development of multi-principal element structural alloys. *Scripta Materialia* **127**, 195–200 (2017).
52. Shanks, H. R., Maycock, P. D., Sidles, P. H. & Danielson, G. C. Thermal Conductivity of Silicon from 300 to 1400 °K. *Physical Review* **130**, 1743–1748 (1963).
53. Schneider, C. A., Rasband, W. S. & Eliceiri, K. W. NIH Image to ImageJ: 25 years of image analysis. *Nature Methods* **9**, 671–675 (2012).

Acknowledgements

Author Contributions

P.B., J.P.S., and J.S. designed the study. P.B., J.L., and S.A.K. fabricated the samples. P.B. and T.M. performed the laser heating experiments and OM imaging. P.B., J.L., and Y.L. performed the XRD measurements. B.E.S. and C.C.B. performed the EDS measurements. J.P.S. performed the temperature profile simulations. J.P.S., J.J.V., and J.S. advised the research. All authors contributed to the data analysis, discussion, and writing of the manuscript.

Additional Information

Supplementary information accompanies this paper at doi:10.1038/s41598-017-07719-2

Competing Interests: The authors declare that they have no competing interests.